NUMERICAL SIMULATION OF ICE ACCRETION ON MULTIPLE-ELEMENT AIRFOIL SECTIONS

Sander J. Jacobs, Jacco M. Hospers, Harry W.M. Hoeijmakers
University of Twente, Enschede, the Netherlands

Keywords: *Subsonic, Weather Effects, CFD*

Abstract

In this study, computational methods are presented that compute ice accretion on multiple-element airfoils in specified icing conditions. The 2DFOIL-ICE numerical simulation method used is based on an incompressible potential flow model coupled with a Lagrangian method for predicting droplet trajectories and the resulting droplet catching efficiency of the surface of the configuration. Flow field and droplet catching efficiency form input for Messinger's model for ice accretion. The EFD-FLOW numerical method obtains the flow field by solving the Euler equations for unsteady compressible inviscid flow on an unstructured grid. This method has been coupled to a Lagrangian method to obtain the spatial distribution of droplet loading and droplet velocity on an unstructured grid. From these quantities the droplet catching efficiency is derived.

For a single-element airfoil a good agreement is found with the ice shapes predicted by other computational methods. Agreement with the experimental ice shapes is fair. The application of the method to a three-element airfoil is described. The comparison of the catching efficiency predicted by both simulation methods is good. The agreement of predicted ice accretions with available experimental data is reasonable.

1 Introduction

Aircraft icing has long been recognized as a serious flight safety problem. According to Petty & Floyd [1], airframe icing cost more than 50 accidents and incidents, claiming more than 800 lives, in the period 1992 – 2000, in the US alone. Icing occurs when super-cooled water droplets hit the aircraft, flying at a level where the temperature is at or below the freezing point. Ice accretion on the wing leading edge or on the tail plane can result in non-aerodynamic shapes and in serious degradation of the aerodynamic performance, such as a decrease in the stall angle, an increase in drag, a decrease in maximum lift, and altered moment characteristics of the aircraft. Also, ice accretion on parts of the engine nacelles or on propellers can cause dangerous situations. Computer simulation of the ice accretion process provides an attractive method for determining the ice shapes on aircraft wings and evaluating a wide range of icing conditions. An ice accretion model that accurately predicts growth shapes on an arbitrary airfoil is valuable for analysis of the sensitivity of airfoils to ice accretion and for analysis of the influence of variables such as airspeed and angle of attack, pressure, temperature, humidity, droplet size, etc. on the accretion process. The predicted ice shapes can be used in wind tunnel and flight tests to assess aircraft performance and handling qualities degradation in icing conditions.

The same model can also be used to assess the energy requirements necessary to prevent ice build-up on an airfoil. Once a model has been validated, it will provide a cost effective means of performing most of the icing research studies which now rely upon experimental techniques.

Nowadays, it is common practice in the aircraft manufacturing industry to apply computational methods for ice accretion in two-dimensional flow for investigating icing. Studies to extend the two-dimensional ice growth model to three-dimensional flows are in progress at for example NASA GRC as well as at CIRA and ONERA. The 2DFOIL-ICE method [2, 3, 4 and 5] predicts the growth of ice on 2D surfaces. It is based on a quasi-steady model that takes into account all important mass and heat transfer processes that occur when super-cooled water droplets strike an airfoil. The droplets either freeze immediately upon impact or freeze partly while the rest of the water runs back on the airfoil. The capabilities of the method have recently been extended by the inclusion of a model for thermal ice protection systems.[4] The use of this method, therefore, not only enables the assessment of potential icing hazards due to ice growth on unprotected surfaces but also the design and appropriate placement of thermal ice protection systems.

Aircraft icing is a threat during take-off and landing, when high-lift devices of the multi-element airfoil are deployed. The geometric capability of the method has recently been extended to the case of multi-element airfoil sections [5].
The objective of the present work is to compare numerical results and experimental data available from literature to the results obtained with 2DFOIL-ICE, for ice accretion calculations for multi-element airfoils, in order to assess its value as an analysis tool for carrying out more studies to further elucidate the pertinent physical phenomena involved in the ice accretion and anti-icing process.
A brief review of the ice accretion model is first presented. Then, the computational procedure is explained briefly. Finally, comparisons with other numerical results and experimental data are made.

2 Ice Accretion

Due to the inertia the trajectories of the super-cooled droplets will deviate from the streamlines, causing the droplets either to impinge on the airfoil or to be carried past it. The size, the shape and the location of the ice that will form depend on:

- the environmental parameters, such as ambient air temperature, pressure, cloud liquid water content (*LWC*), relative humidity and the median volumetric droplet diameter (*MVD*);
- the aircraft surface conditions, such as surface temperature, roughness and the surface tension at the air/water interface;
- the flow parameters, such as the flight velocity, angle of attack and the icing time.

Two distinct types of ice accretion have been observed:

- Rime-ice accretions: a dry, opaque and milky-white ice deposit with a density lower than that of the impinging droplets. It usually occurs at lower airspeeds, lower temperatures and lower *LWC*'s. In rime ice conditions the released latent heat of freezing is insufficient to raise the local temperature above the freezing point and all the droplets freeze fully upon impact. Generally, the rime-ice accretions have a streamlined shape.
- Glaze-ice accretions: a heavy coating of a transparent ice which spreads over the wing and has a density close to that of the impinging droplets. It usually develops at higher airspeeds, temperatures closer to the freezing point and higher *LWC*'s. In glaze-ice conditions, due to the relatively high amount of released latent heat of freezing, only part of the water in the droplets freezes upon impact, the rest runs back along the airfoil surface. Generally, the ice formations have an irregular, non-aero-dynam-ical shape which may jeopardize the aerodynamic characteristics of the air-foil section.

3 Droplet Distribution

It is assumed that the droplets form a dilute mono-disperse distribution, so that the droplet trajectories do not affect each other, so the effects of collisions are neglected. The following further assumptions are made when considering the motion of an isolated droplet moving in a steady, non-uniform velocity field:

- the droplets are so small (10-50 μm) that the velocity field induced by the airfoil in absence of the droplets can be used, i.e. one-way coupling is employed;
- the density of the liquid in the droplet remains constant;
- the droplet volume remains constant, implying that evaporation or condensation do not take place, nor break-up or coalescence, nor splashing;
- droplets are spheres, with a diameter equal to the equi-volumetric diameter d_{eq}, the diameter of a spherical droplet with the same volume;
- far upstream the droplet velocity equals the free stream velocity.

Droplets released upstream of the airfoil will tend to follow the streamlines up to some distance to the airfoil. Closer to the airfoil the flow will no longer be uniform. Due to the difference in density of the water and that of air, the changes in air velocity the droplet trajectories start to deviate from the streamlines. Since the relative velocity is low and the droplet size is small the flow around the droplet is a low-Reynolds-number flow. In considering the relative flow around a droplet, up to six different contributions to the force exerted on the droplet can be distinguished: the steady-drag force, the steady-lift force, the added-mass force, the pressure gradient force, the Basset motion history force and the buoyancy force. Typically the steady-drag force is dominating the interaction forces and usually only this force and the buoyancy force (though very small) are used in Newton's second law that governs the droplet trajectory, i.e.

$$\frac{d\vec{x}_d}{dt} = \vec{u}_d \tag{1a}$$

$$m_d \frac{d\vec{u}_d}{dt} = \vec{D} + (\rho_d - \rho_a) V_d \vec{g} \tag{1b}$$

In Eq. (1) $\vec{D} = \frac{1}{2}\rho_a A_d C_D |\vec{u} - \vec{u}_d| (\vec{u} - \vec{u}_d)$ is the drag force experienced by the droplet, m_d is the droplet mass, ρ_d the droplet density, V_d the droplet volume, ρ_a the density of the air, $\vec{g}$ the acceleration of the gravity, A_d the droplet frontal area, C_D the drag coefficient of the droplet, $\vec{u}$ the local velocity of the air stream and $\vec{u}_d$ the velocity of the droplet. Eq. (1) can be rearranged into:

$$\frac{d\vec{x}_d}{dt} = \vec{u}_d \tag{2a}$$

$$\frac{d\vec{u}_d}{dt} + \frac{C_D \,\mathrm{Re}_d}{24} \frac{18\mu_a}{d_{eq}^2 \rho_d} (\vec{u}_d - \vec{u}) = (1 - \frac{\rho_a}{\rho_d})\vec{g} \tag{2b}$$

where $\mathrm{Re}_d = \rho_a |\vec{u} - \vec{u}_d| d_{eq} / \mu_a$ is the droplet Reynolds number. In very viscous (Stokes') flow the drag coefficient of a sphere is $C_D = 24/\mathrm{Re}_d$.

However, in flows relevant to ice accretion the Reynolds numbers are not very low and a modified expression for the drag coefficient is used:

$$\frac{C_D \,\mathrm{Re}_d}{24} = 1 + 0.197\,\mathrm{Re}_d^{0.63} + 2.6 \times 10^{-4}\,\mathrm{Re}_d^{1.38} \tag{3}$$

This expression is accurate for Reynolds number up to 1000. The Reynolds numbers encountered in the applications do not exceed 100. Note that making Eq. (2) non-dimensional, using $L_{ref} = c$, $U_{ref} = U_\infty$, $t_{ref} = c/U_\infty$, we find

$$\frac{d^2\vec{\xi}_d}{d\tau^2} + K(\frac{d\vec{\xi}_d}{d\tau} - \frac{\vec{u}}{U_\infty}) = (1 - \frac{\rho_a}{\rho_d})\frac{\vec{g}c}{U_\infty^2} \tag{4}$$

where $\vec{\xi}_d = \vec{x}_d / L_{ref}$, $\tau = t/t_{ref}$ and

$$K = 18 \frac{C_D \,\mathrm{Re}_d}{24} \frac{\rho_a}{\rho_d} \frac{1}{\mathrm{Re}_c} \frac{1}{(d_{eq}^2 / c^2)}$$

with $\mathrm{Re}_c = \rho_a U_\infty c / \mu_a$, the airfoil Reynolds number. It shows that, apart from the density ratio ρ_a/ρ_d and the Froude number ($Fr^2 \equiv U_\infty^2 / c|\vec{g}|$), the Langmuir parameter K is an important parameter. K represents the ratio of the viscous drag force and the inertial term: for large values of K the droplet velocity $\vec{u}_d$ will tend to the air velocity $\vec{u}$ and the droplets will follow the streamlines. This implies that relatively small droplets ($d_{eq}/c << 1$), i.e. for large wings, icing will not be an important issue. However, for smaller aircraft, or for smaller parts of larger aircraft, icing will be important.

4 Ice Accretion Model and Thermodynamics

4.1 Control Volume for liquid flow

The amount of ice that accretes on the airfoil is computed by solving the heat and mass balances for small shallow control volumes that are located along the (iced) airfoil surface. The physical model used in the present method is Messinger's method [6], applied in most present-day ice accretion prediction methods.

The equations that describe the thermodynamics of the freezing process are obtained by applying

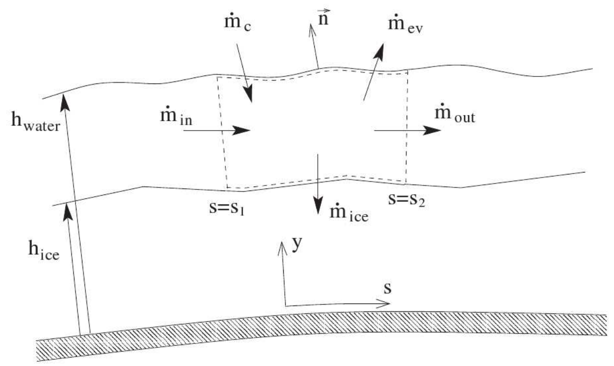

Fig. 1 Control volume, definition mass flow rates

the continuity equation and energy conservation equation, for steady flow and constant mass flow rates, to a small shallow control volume. The control volume is within the boundaries $s = s_1$, $y = h^{-}_{water}(s)$, $s = s_2$, $y = h^{+}_{ice}(s)$, where s is the coordinate along the surface, see Fig.1. The + and - sign indicate that the control volume boundary is just above and just below the interface, respectively. The two chord-wise boundaries coincide with the edges of the panels that constitute the airfoil. The lower boundary of the control volume is initially on the surface of the clean geometry, and moves outward with the surface as the ice accretes. Therefore, the control volume is always situated on either the clean or on the iced surface, and any accumulated ice is considered to leave the control volume through the lower boundary.

It should be noted that h_{ice} and h_{water} vary with time as a consequence of the ice accretion, but that they remain at the same relative distance due to the assumption of steady flow and constant mass flow rates.

For dimensional completeness, the control volume is considered to extend one unit length in the span-wise direction.

It is assumed that the control volume is so small that all physical variables can be taken constant in the control volume. The only terms representing the motion of the water on the surface that are taken into account are $\dot{m}_{in}$ and $\dot{m}_{out}$, i.e. the rate of water flowing into the control volume from of the upstream one and the rate of water flowing out of the control volume into the downstream one, respectively, both [kg/ms], that is [kg/s] per meter span. This means that there is a water transport along the surface, but it is assumed that the velocity of the water is so small that it can be neglected. This assumption is valid in cases the water layer is thin. As a consequence of this assumption the equation describing conservation of momentum of the liquid water in the control volume is not used.

4.2 Conservation of Mass

The conservation of mass for water in an arbitrary control volume V with boundary ∂V moving with velocity $\vec{u}_{\partial V}$ is (2D):

$$\frac{\partial}{\partial t}\iint_V \rho_w dV + \int_{\partial V} \rho_w[(\vec{u}_w - \vec{u}_{\partial V}).\vec{n}]dS = 0 \qquad (5)$$

where $\vec{n}$ is the unit normal vector on the surface of the control volume, pointing outwards. Using the assumption of quasi-steadiness, the unsteady term drops out and, because of constant mass flow rates ($\vec{u}_{\partial V}$ = constant in V), it follows

$$\int_{\partial V} \rho_w(\vec{u}_w.\vec{n})dS - \rho_w \vec{u}_{\partial V} \cdot \int_{\partial V} \vec{n} dS = 0 \qquad (6)$$

which because ∂V is a closed surface reduces to

$$\int_{\partial V} \rho_w(\vec{u}_w.\vec{n})dS = 0 \qquad (7)$$

The contributions to the contour integral term are $\dot{m}_{in}$, the mass flow of runback water into the control volume and $\dot{m}_{out}$ the mass flow of runback water out of the control volume, assuming that the variables are constant on each boundary of the control volume, i.e.,

$$\dot{m}_{in} = \int_{h^{+}_{ice}}^{h^{-}_{water}} \rho_w u_{in} dy \Big|_{s=s_1} \qquad (8)$$

and

$$\dot{m}_{out} = \int_{h_{ice}^{+}}^{h_{water}^{-}} \rho_w u_{out} dy \Big|_{s=s_2} \tag{9}$$

To determine the contribution from the lower and upper boundary of the control volume, one has to perform a contour integral once again. The corresponding control volume is an infinitesimal control volume located on the interface, partially in the water and partially in the ice, or partially in the water and partially in the air. Such a control volume analysis couples the conditions on both sides of the interface. It is assumed that splashing does not take place and that the phase changes are instantaneous. The rate of ice that is formed is denoted by $\dot{m}_{ice}$, while the rate at which water evaporates at $y = h_{water}$ is denoted by $\dot{m}_{ev}$.

The mass flow rate into the control volume due to the droplets caught by the surface is expressed by

$$\dot{m}_c = (LWC)U_\infty \beta \Delta s \tag{10}$$

Here, LWC is the liquid water content of the ambient air [kg/m^3] and Δs is the length of the control volume along the surface [m]. β is the dimensionless local catching efficiency, defined as the ratio, for a given mass of water, of the area of impingement to the area through which the same water passes at some distance upstream of the airfoil. The catching efficiency is derived from droplet trajectories starting in the uniform flow upstream of the airfoil that impact the airfoil.

The mass flow rate due to evaporation can be expressed in terms of the local temperature and pressure. In case there is no water on the surface there will be no evaporation. However, in that case, water can still leave the surface through sublimation of ice and $\dot{m}_{ev}$ is replaced by $\dot{m}_{sub}$, the rate of mass transfer through sublimation.

The mass balance then becomes

$$-\dot{m}_{in} + \dot{m}_{out} - \dot{m}_c + \dot{m}_{ev} + \dot{m}_{ice} = 0 \tag{11}$$

All terms are in units of [kg/ms], that is [kg/s] per meter span.

The concept of a freezing fraction can be used to determine the type of process taking place within the control volume. The freezing fraction, f, was defined by Messinger [3] as the fraction of impinging liquid that freezes within the region of impingement, i.e.,

$$f = \frac{\dot{m}_{ice}}{\dot{m}_c} \tag{12}$$

The remaining water runs along the surface. In the present study, f is defined as the fraction of the total mass of water entering the control volume that freezes within the control volume. It is given by

$$f = \frac{\dot{m}_{ice}}{\dot{m}_c + \dot{m}_{in}} \tag{13}$$

For colder (rime) icing conditions, the droplets tend to freeze immediately on impact, resulting in zero runback. In that case, neglecting sublimation, the freezing fraction equals 1.0. Freezing fractions equal to 0.0 indicate that no ice has formed in the control volume. Freezing fractions between 0.0 and 1.0 characterize glaze ice or ice that has some combination of glaze and rime characteristics. The local value of f can vary along the surface, and can be calculated from the control-volume mass and energy balance. Fig.2 shows the three phase-regimes that can be distinguished. The freezing fraction acts as a phase-regime indicator.

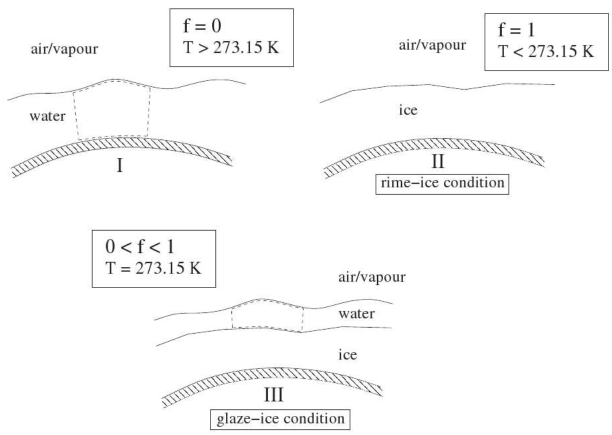

Fig. 2 Three possible phase-regimes

4.3 Conservation of Energy

The conservation of energy within the control volume can be expressed in a similar way as the conservation of mass. In the energy equation the work done by frictional forces within the water and the work done by external force fields are neglected, while it is assumed that there are no volumetric heat sources. This leads to:

$$\int_{\partial V} \rho_w H_w (\vec{u}_w.\vec{n}) dS = -\int_{\partial V} \vec{q}_w.\vec{n} dS \tag{14}$$

with H_w the total enthalpy and $\vec{q}_w$ the heat flux vector. When considering the enthalpy of the runback water that flows into the control volume, out of the upstream control volume, the kinetic energy is not taken into account, i.e.

$$\dot{m}_{in} H_{w,in} = \int_{h_{ice}^+}^{h_{water}^-} \rho_w h_{w,in} u_{in} dy \Big|_{s=s_1} \tag{15}$$

Similarly, in the enthalpy of the water leaving the control volume, the kinetic energy is not taken into account,

$$\dot{m}_{out} H_{w,out} = \int_{h_{ice}^+}^{h_{water}^-} \rho_w h_{w,out} u_{out} dy \Big|_{s=s_2} \tag{16}$$

An expression for the contributions associated with droplet catching, evaporation and freezing is obtained from the control volume analysis for a control volume containing the interface. The heat flux due to convection at the air/water interface:

$$q_{conv} \Delta s = \int_{s_1}^{s_2} \vec{q}_{conv,w}.\vec{n} ds \Big|_{h=h_{water}^-} \tag{17}$$

Note that though the convective heat flux is commonly referred to as ‘convective’, it follows from a heat conduction term.

It is assumed that the radiative heat flux can be neglected, while also the heat flux through the boundary at $s = s_1$ and the one at $s = s_2$ due to conduction can be neglected. There is no heat flux through the lower boundary of the control volume, since as soon as ice has accreted any heat transfer between the water and the ice and between the ice and the airfoil skin will be very small since ice is an insulator. In case both ice and water are present on the airfoil, the temperature of the ice and the water will be both 273.15 K and there will be no convective heat flux between the water and the ice. The right-hand side of Eq. (14) is then

$$-\int_{\partial V} \vec{q}_w.\vec{n} dS = -q_{conv} \Delta s \tag{18}$$

with

$$q_{conv} = h_c \left[T_{sur} - \left(T_e + r \frac{U_e^2}{2c_{p,a}} \right) \right] \tag{19}$$

the convective heat flux per unit area [W/m^2], with h_c the convective heat transfer coefficient and r the recovery factor. T_e and U_e are the temperature and velocity outside the control volume at the edge of the air boundary layer, respectively. The local temperature T_e is calculated from the pressure calculated by the potential flow method using the isentropic relations. T_{sur} is the temperature of the water in the control volume. Δs is the length of the control volume along the surface. Substituting and writing out the different terms, assuming the specific heat of water ($c_{p,w}$) and that of ice ($c_{p,i}$) to be constant, and using Eq. (11), we find

$$\begin{aligned} &\dot{m}_{ev} h_{WV/IV}^{T_{ref}=T} + q_{conv}\Delta s = \\ &\dot{m}_c \left[c_{p,w}(T_\infty - T) + \tfrac{1}{2} U_\infty^2 \right] \\ &\quad + \dot{m}_{in} \left[c_{p,w}(T_{in} - T) \right] \\ &+ \dot{m}_{ice} h_{IW}^{T_{ref}=T_f} - \dot{m}_{ice} c_{p,w}(T_f - T) \\ &\quad + \dot{m}_{ice} c_{p,i}(T_f - T) \end{aligned} \tag{20}$$

with $T_f = 273{:}15$ K. T_{ref} is the reference temperature and $T = T_{sur} = T_{out}$. The subscript (w) denotes the water phase, the subscript (v) denotes the vapour phase, the subscript (i) denotes the ice phase, and the subscript (a) denotes the property of air. $h_{WV}^{T_{ref}=T}$ is the latent heat of vaporisation of water at temperature T, $h_{IV}^{T_{ref}=T}$ is the latent heat of sublimation. All terms are in units of [W/m], that is [W] per meter span.

With reference to Vukits [7], Eq. (20) is expressed in the form

$$\dot{Q}_{Source} = \dot{Q}_{Sink} \tag{21}$$

where $\dot{Q}_{Source}$ represents the heat flux from sources and $\dot{Q}_{Sink}$ represents the heat flux from sinks. A source provides heat to the control volume. A sink represents a process that removes heat from the control volume.

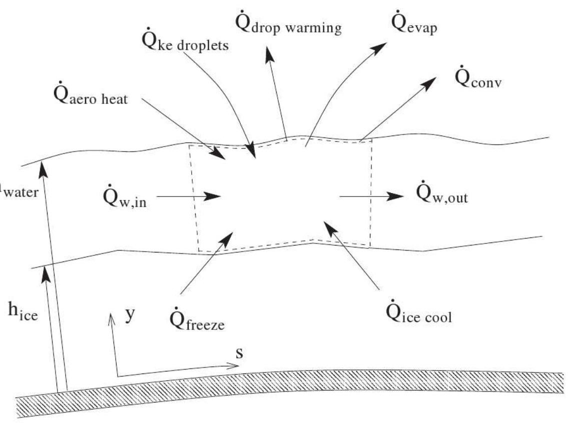

Fig. 3 Heat fluxes within control volume

Assuming that the surface skin temperature is higher than the temperature of the air and the droplets ($\dot{Q}_{dropwar\min g}$ is a sink), the sources of heat are (see Fig.3),

$$\dot{Q}_{Source} = \dot{Q}_{in} + \dot{Q}_{freeze} + \dot{Q}_{aeroheat} + \dot{Q}_{ke\ droplets} + \dot{Q}_{icecool}(+\dot{Q}_{anti-ice}) \quad (22)$$

where

$$\dot{Q}_{in} = \dot{m}_{in}\left[c_{p,w}(T_{in} - T)\right]$$

$$\dot{Q}_{freeze} = \dot{m}_{ice} h_{IW}^{T_{ref}=T_f} + \dot{m}_{ice} c_{p,w}(T - T_f)$$

$$\dot{Q}_{kedroplets} = \dot{m}_c\left[\tfrac{1}{2}U_\infty^2\right]$$

$$\dot{Q}_{icecool} = -\dot{m}_{ice} c_{p,i}(T - T_f)$$

$$\dot{Q}_{aeroheat} = h_c(T_e + r\frac{U_e^2}{2c_{p,a}} - T_\infty)\Delta s$$

Again, $T = T_{sur} = T_{out}$. The heat flux due to conduction, $\dot{Q}_{anti\text{-}ice}$, comes into play in the anti-icing model. The heat sinks are as follows (see Fig.3),

$$\dot{Q}_{Sink} = \dot{Q}_{conv} + \dot{Q}_{drop\ warming} + \dot{Q}_{evap} + \dot{Q}_{out} \quad (23)$$

where

$$\dot{Q}_{conv} = h_c(T_{sur} - T_\infty)\Delta s$$

$$\dot{Q}_{drop\ warming} = \dot{m}_c c_{p,w}(T_{sur} - T_\infty)$$

$$\dot{Q}_{evap} = \dot{m}_{ev} h_{WV}^{T_{ref}=T_{sur}}$$

$$\dot{Q}_{out} = \dot{m}_{out} c_{p,w}(T_{out} - T_{sur})$$

All terms substituted in Eq. (21) yields:

$$\dot{Q}_{in} + \dot{Q}_{freeze} + \dot{Q}_{aeroheat} + \dot{Q}_{ke\ droplets} + \dot{Q}_{icecool}(+\dot{Q}_{anti-ice}) = \dot{Q}_{conv} + \dot{Q}_{drop\ warming} + \dot{Q}_{evap} + \dot{Q}_{out} \quad (24)$$

5 Numerical Approaches

As soon as ice starts to accrete on the airfoil, the flow around the airfoil will change because of the change in shape of the iced airfoil. In turn a different flow field will lead to a change in the ice accretion process, since there will be an influence on the droplet trajectories, the catching efficiency, the convective heat transfer coefficient, etc. This implies that the ice accretion process is a time-dependent process and requires the solution of time-dependent equations. However, the changes in time are slow and we adopt a quasi-steady approach in which the ice accretion is computed layer by layer, assuming a steady flow field during the growth of each layer. The algorithm consists of four steps:

- compute the flow field by potential-flow method or by method based on Euler equations;
- compute the droplet catching efficiency, by a Lagrangian or an Eulerian method
- solve the mass and the heat balances along the airfoil surface;
- define a new, iced, airfoil shape.

5.1 Computation of the Flow Field

Starting with the appropriate airfoil and environmental data, the flow field around the airfoil is calculated. At high Reynolds number, low Mach number and for not too ragged ice shapes the flow around the airfoil section may be described by an inviscid flow method. In section 5.1.1 an incompressible potential flow model is described, which is governed by Laplace's equation for the velocity potential. In section 5.1.2 an alternative inviscid flow method is described: the one based on Euler's equations for (compressible) inviscid flow, which does not require the assumption of irrotational flow.

5.1.1 Potential-Flow Method

The computational method 2DFOIL [2, 3, 4 and 5] is used to compute the potential flow field around the airfoil. 2DFOIL is a second-order accurate panel method for the two-dimensional unsteady, incompressible potential flow around arbitrary airfoil shapes. An airfoil cross section is divided into a large number of (curved) segments of varying lengths, employing a curvature-dependent paneling scheme. Considerably more airfoil segments are defined near the leading edge where ice accretion is anticipated.

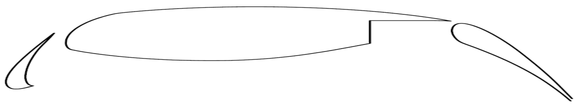

Fig. 4 Multi-element airfoil section

The main challenge in extending the method to deal with realistic, multi-element airfoils is the modeling of the flow inside the “coves”, i.e. the regions just downstream of the sharp edges on the lower surfaces of the slat and the main airfoil, see Fig. 4, which clearly cannot be modeled by an inviscid potential flow method. The problem is solved by defining “cove bounding streamlines”, which are subsequently input as airfoil surface, thus extending the airfoil to include the cove. Consider as an example of such an extension the slat, see Fig. 5.

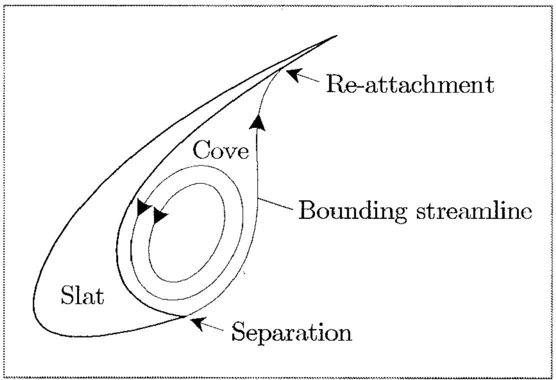

Fig. 5 Approximate streamline covering the cove region of a slat

It is assumed that the cove-bounding streamline is a free streamline, along which the pressure is constant, presumably close to atmospheric pressure. The free streamline is assumed to re-attach to the surface before it reaches the trailing edge. In the present version of 2DFOIL-ICE the location and shape of a cove bounding streamline must be defined by the user. The bounding streamline is a fifth-degree curve in terms of the arc length along the curve. The curve is fixed by specifying the location of the separation point and the re-attachment point, as well as the first and second derivative at these two points. The latter are usually chosen such that at the separation and the re-attachment point the slope and curvature of the bounding stream line coincide with those of the solid surface. Then, with the

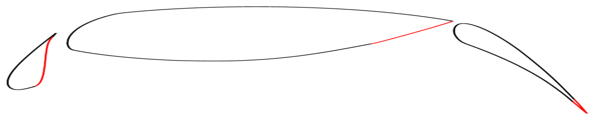

Fig. 6 Modified section with approximate streamlines covering the cove regions

separation point at the sharp edge, the only parameters are the re-attachment point and the length of the bounding streamline. These are chosen by trial and error, such that the static pressure is more or less constant along the bounding streamline. This method is discussed in detail in Ref. 5. Fig. 6 shows for the configuration of Fig. 4 the result of this procedure 2DFOIL employs a panel-wise linear source distribution, a panel-wise quadratic doublet distribution and accounts for the curvature of the surface. The singularity distributions are solved for by imposing the Dirichlet condition that in the interior of each of the elements of the airfoil section the perturbation potential equals zero, at the midpoint of each panel. The velocities around the airfoil and on the airfoil surface follow from the calculated source and doublet distribution.

Panel methods are known to be very reliable numerical tools to compute the flow field and the pressure distribution in regions away from the airfoil or at specific points on the airfoil itself such as the collocation points. Care should be taken when the panel method is used to compute the droplet trajectories close to the paneled surface of the airfoil, since only at the collocation points the zero-normal-velocity boundary condition is met exactly. Away from the collocation points a nonzero normal velocity may arise. Furthermore, close to the panel edges the discontinuities in the geometry and in the singularity distributions result in a (logarithmic) singular velocity field, i.e. in a locally very high, unrealistic, value of the velocity. In the present higher-order panel method this problem is considerably less severe than for lower-order panel methods. The problem is further reduced by pursuing the following approach. If a droplet is within a certain distance (determined to be three panel widths) away from the airfoil, the nearest panel and its two neighbors are each divided in N sub-panels. The parameters required in the definition of the linear source and quadratic doublet distribution on the sub-panels are obtained from the computed source and doublet distribution on the original panels by linear and quadratic interpolation, respectively. Subsequently the velocity induced by the (known) singularity distributions on the sub-paneled geometry is computed, which yields a smooth behavior of the velocity along the trajectory.

5.1.2 Flow Model based on Euler's Equations

The incompressible potential flow method will become inaccurate in case of higher free-stream velocities for which effects of compressibility start to play a role. Furthermore, strong viscous flow effects, such as flow separation and associated occurrence of rotational flow, cannot be handled accurately within the framework of potential-flow. Strong viscous flow effects are important within the flow field around multiple-element airfoil sections, e.g. in the cove regions and in region where the wake from an upstream element merges with the boundary layer of a downstream element. In the present study a first step is made towards compressible viscous-flow modeling, by employing a numerical method based on the Euler equations for three-dimensional unsteady, inviscid, compressible flow. In this method it is assumed that air is a calorically perfect gas.

The Euler equations for conservation of mass, momentum and energy are solved using a finite volume scheme for an unstructured hybrid grid. For the present 2D applications, the grid consists of triangular and quadrilateral elements. The latter are required for future extension of the numerical method from the flow model using the Euler equations to the flow model based on the Navier-Stokes equations. The choice of the unstructured grid over a (block-) structured grid allows the relatively easy application to complex geometries and allows future implementation of grid adaptation. In the present method we used a so-called median dual mesh as control volumes is constructed from the unstructured grid, see [8].

The flow field quantities are assumed to be steady and follow from the discretised version of Euler equations by integrating in time, using an explicit Runge-Kutta scheme, until the solution becomes independent of time. The numerical scheme used for the unstructured-grid discretisation of the flux terms in the Euler equations is the approximate Riemann solver described in [9]. It is the HLLC scheme, proposed by Harten, Lax and van Leer [10], with modifications due to Toro [11] and Batten et al. [12] for implementation on unstructured grids, combined with the (Advection-Upstream-Splitting Method) AUSM+ scheme, proposed by Liou and Steffen [13], with extensions described in [14] and [15]. Second-order spatial accuracy is obtained by the MUSCL (Monotone Upstream-Centred Scheme for Conservation Laws of van Leer [16]) type scheme with the limiter, designed for unstructured grids, of Barth & Jespersen [17] and of Venkatakrishnan[18]. The resulting method is designated the EFD-FLOW method.

The EFD-FLOW method is an inviscid-flow method, which implies that flow separation is not modeled, in principle. However, it is well-accepted that flow separation from sharp trailing edges as occurs in solutions of the discretised Euler equations mimic reality. However, this is not true for the separated flow region that occurs in the cove regions of the multiple-element airfoil. Therefore, for the multiple-element airfoil we used the same faired-over cove regions as employed for the potential-flow method.

5.2 Droplet Catching Efficiency - Lagrangian

Droplet trajectories are calculated in the potential flow field using the appropriate mean cloud droplet diameter. From the location of the impacts of the various trajectories on the airfoil, local values of water droplet catching efficiency are calculated around the airfoil.

The droplet trajectories are obtained from Eq. (2), using Eq. (3), employing a five-stage Runge-Kutta scheme to integrate the equations in time. The time step in the method is adapted such that the CFL condition is satisfied: the time step is smaller than a specified maximum depending on the local magnitude of the velocity, resulting in the position of the droplet does not changing more than a specified maximum. The time step also depends on the curvature of the trajectory.

A droplet is considered to have impacted when its trajectory intersects one of the panels. To determine the impact point the droplet velocity at the point on the trajectory just prior to intersection is used to extrapolate the droplet trajectory to the surface.

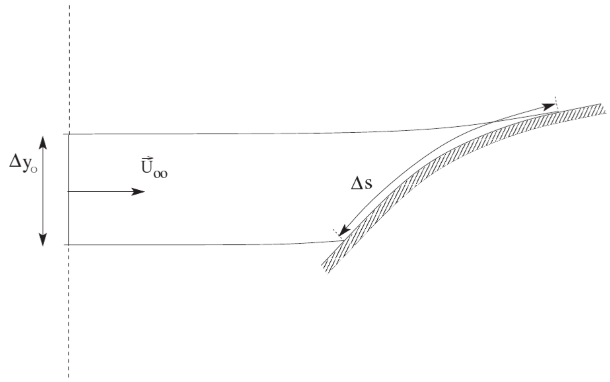

Fig. 7 Determination of catching efficiency β

First, per element of the airfoil, the two limiting droplet trajectories are determined, one that just hits the upper surface and one that just does not miss the lower surface. For this purpose droplets are released upstream of the leading edge of the airfoil, at a location where the flow is approximately uniform with velocity equal to $\vec{U}_\infty$.

Next, a number of closely-spaced droplets is released, also far upstream, in between the starting points of the lower and upper limiting trajectories and the impact points on the airfoil (element) are determined. The amount of water passing through the line segment between two successive droplet trajectories equals, see Fig. 7, $\vec{U}_\infty.(\vec{e}_n \times \vec{e}_z)\Delta n(LWC)$ [kg/ms], with $\vec{e}_n \Delta n$ the distance between the starting points of two consecutive droplet trajectories. In the example in Fig. 7, $\vec{e}_n \Delta n = \Delta y_o \vec{e}_y$. This amount of water hits the airfoil locally over a length Δs, as was given in Eq. (10) as $\beta U_\infty \Delta s(LWC)$, so that

$$\beta(s) = \frac{\vec{U}_\infty.(\vec{e}_n \times \vec{e}_z)}{U_\infty} \frac{\Delta n}{\Delta s} \tag{25}$$

Since we known the relation between location of the starting point of the droplet trajectory and the s-coordinate at which the droplet hits the airfoil surface, i.e. s(n), we can determine the local catching efficiency $\beta(s)$ by finding, at each impact point, the derivative of n(s) from the spline-fit through the impact point and its immediate neighbors. At the two end points, which determine the impingement region, β becomes zero. Finally, the value of β at the panel midpoints is obtained by linear interpolation between the values of β found at the two nearest impact points.

5.3 Droplet Catching Efficiency - Eulerian

For the Lagrangian method a large number of droplets has to be released and tracked to determine whether or not droplets impinge on the airfoil surface, i.e. to find the limiting droplet trajectories, in between which the droplets are released in order to calculate the droplet catching efficiency. This is specifically true for complex geometries, such as multi-element airfoils, for which several regions of the configuration may be wetted. An alternative to the Lagrangian method is the Eulerian method, see e.g. [19]. The present Eulerian method solves, for a given flow field $\vec{u}(\vec{x})$, for the droplet velocity $\vec{u}_d$ and droplet loading Φ in a computational domain around the configuration using the finite-volume discretisation method. In order to deal with complex configurations the method is implemented on an unstructured grid consisting of triangles.

Assuming that in a small control volume there are still a large number of droplets present, the partial differential equations governing the liquid flow are the conservation of mass:

$$\frac{\partial}{\partial t}(\alpha\rho_d) + \vec{\nabla}.(\alpha\rho_d\vec{u}_d) = 0 \tag{26a}$$

and conservation of momentum:

$$\frac{\partial}{\partial t}(\alpha\rho_d\vec{u}_d) + \vec{\nabla}.(\alpha\rho_d\vec{u}_d\vec{u}_d) = \alpha\rho_d \vec{f}_{drag} + \alpha(\rho_d - \rho_a)\vec{g} \tag{26b}$$

,

respectively, with α the volume fraction of the liquid. In Eq. (26b) the drag force $\vec{f}_{drag}$ is the drag force per unit mass of the liquid, which follows from Eq. (1) as

$$\vec{f}_{drag} = \frac{\vec{D}}{\rho_d V_d} = \tfrac{1}{2}\rho_a |\vec{u}-\vec{u}_d|(\vec{u}-\vec{u}_d)\frac{C_D A_d}{\rho_d V_d}$$

$$= \frac{C_D \operatorname{Re}_d}{24}\frac{18\mu_a}{d_{eq}^2 \rho_d}(\vec{u}-\vec{u}_d)$$

with $A_d = \frac{\pi}{4}d_{eq}^2$, $V_d = \frac{\pi}{3}d_{eq}^3$, $\operatorname{Re}_d = \frac{\rho_a |\vec{u}-\vec{u}_d| d_{eq}}{\mu_a}$

We define the liquid loading as $\Phi = \alpha\rho_d$, which equals the mass of water per unit volume, i.e. it can be interpreted as the distribution of the liquid water content of the air, with LWC its free-stream value. The governing equations, Eq. (26), then become:

$$\frac{\partial}{\partial t}(\Phi) + \vec{\nabla}.(\Phi\vec{u}_d) = 0 \tag{27a}$$

$$\frac{\partial}{\partial t}(\Phi\vec{u}_d) + \vec{\nabla}.(\Phi\vec{u}_d\vec{u}_d) = \Phi\vec{f}_{drag} + \Phi(1-\frac{\rho_a}{\rho_d})\vec{g} \tag{27b}$$

Combining Eqs. (27a) and (27b) yields:

$$\frac{\partial}{\partial t}(\vec{u}_d) + (\vec{u}_d.\vec{\nabla})\vec{u}_d = \vec{f}_{drag} + (1-\frac{\rho_a}{\rho_d})\vec{g} \tag{28}$$

Multiplication by the constant liquid density ρ_d then gives:

$$\frac{\partial\rho_d\vec{u}_d}{\partial t} + (\rho_d\vec{u}_d.\vec{\nabla})\vec{u}_d = \rho_d\vec{f}_{drag} + (\rho_d-\rho_a)\vec{g} \tag{29}$$

Eqs. (28) and (29) do not involve $\vec{u}_d$ and are PDE's that could be solved decoupled from Eq. (27a). However, neither Eq. (28) nor Eq. (29) is in conservation form like Eqs. (27).
Note that Eq. (28) can also be derived directly from Eq. (2b) for the droplet velocity $\vec{u}_d$. This quantity is considered as a quantity that moves with the particle through the flow field. This implies that the time derivative in Eq. (2b) equals $\frac{d\vec{u}_d}{dt} = \frac{\partial\vec{u}_d}{\partial t} + (\frac{d\vec{x}_d}{dt}.\vec{\nabla})\vec{u}_d$, which with $\frac{d\vec{x}_d}{dt} = \vec{u}_d$ leads to Eq. (28).

Eqs. (27a) and (27b) are solved, for given flow field velocity $\vec{u}$, using a finite volume scheme, in which Eqs. (27) are integrated over a control volume associated with the grid. In case the flow field velocity is obtained from the potential-flow solution, a computational domain is discretised in the form of an unstructured grid. The flow field quantities at the grid points are then computed from the potential-flow solution. In case the flow field follows from the Euler method the same grid is used as the one used for the flow field computation.

In the present method we used the median dual mesh constructed from the triangular mesh as control volumes, see [8], i.e. the same method as used for the numerical method to solve Euler's equations. The droplet loading Φ and velocity $\vec{u}_d$ are flow field quantities that are steady and follow from the discretised version of Eqs. (27) by integrating in time, using an explicit Runge-Kutta scheme, until the solution becomes independent of time. It turns out that this iteration procedure for $\vec{u}_d$ and Φ converges fairly fast. The numerical scheme used for the unstructured-grid discretisation of the flux terms in Eqs. (27) is the same scheme as used for solving Euler's equation for the flow-field quantities, see section 5.1.2.

The system of equations, Eqs. (27), is hyperbolic, with its four wave speeds all equal to $\vec{u}_d$, which facilitates an easy way to determine whether a boundary is an inflow or an outflow boundary and boundary conditions have to be specified or extrapolated from the computational domain, respectively. At the far-field inflow boundary the droplet loading Φ is set equal to LWC, while the droplet velocity $\vec{u}_d$ is set equal to $\vec{u}_d = \vec{u}$. On the part of the airfoil surface for which $\vec{u}_d.\vec{n} > 0$, with $\vec{n}$ the unit external normal on the airfoil surface, is positive, i.e. the part of the airfoil surface that is an outflow boundary, the droplet loading Φ is set equal to zero and the droplet velocity $\vec{u}_d$ is set equal to $\vec{u}_d = \vec{0}$.
The initial condition is that the droplet loading Φ is equal to LWC and the droplet velocity $\vec{u}_d$ is equal to $\vec{u}_d = \vec{u}$.

The distribution of the droplet velocity $\vec{u}_d$ and the droplet loading Φ obtained along the part of the airfoil surface with $\vec{u}_d.\vec{n} < 0$ are used to calculate the local catching efficiency *β(s)*. The amount of water impinging on the airfoil surface is: $-\Phi(\vec{u}_d.\vec{n})\Delta s$. Equating this to the expression given in Eq. (10) $\dot{m}_c = (LWC)U_\infty \beta \Delta s$ then yields

$$\beta(s) = -\frac{\Phi(\vec{u}_d.\vec{n})}{U_\infty LWC} \tag{30}$$

For complex geometries, such as multiple-element airfoils, this approach can be simpler and faster than the Lagrangian approach. Furthermore, extension of the Lagrangian method to three-dimensional configurations is more straightforward than for the Eulerian method.

5.4 Convective Heat Transfer

In the heat balance of the Messinger model the heat transfer coefficient is required. The convective heat transfer coefficient h_c follows from the boundary layer properties. In the present method linear interpolation in the tangential velocity component is used to find the stagnation point. During (glaze) ice accretion irregular shapes may evolve for which a potential flow method produces questionable results, such as the appearance of multiple stagnation points and regions with high velocities. In order to cope with the multiple stagnation points the present method uses the following approach: on each new layer of ice all points where the tangential velocity is zero are determined. The stagnation point on the new layer is chosen as the point closest to the stagnation point on the old ice shape.

Employing the Reynolds analogy, the heat convection coefficient is obtained from the Blasius expression for the turbulent flat-plate boundary layer,

$$h_{c,BL}(s) = 0.0296\,\hat{f}\,\frac{\kappa}{s}\mathrm{Pr}^{1/3}\,\mathrm{Re}_s^{4/5} \tag{31}$$

In Eq. (31) κ is the heat-conduction coefficient of air, *Pr* is the Prandtl number $\mathrm{Pr} = \mu_a c_{p,a}/\kappa$. Re_s is the Reynolds number $\mathrm{Re}_s = \rho_a U_e(s)s/\mu_a$, based on the distance *s* from the stagnation point, and the local velocity from the potential-flow method. The (roughness) factor $\hat{f}$ has been chosen equal to 2, which gave the best agreement between calculated ice shapes and ice shapes found in experiments.

Expression Eq.(31) is applicable in the region of the airfoil not close to the leading edge. Around the stagnation point, a different expression for h_c is used. The nose of the airfoil is approximated by a 2D cylinder with diameter D, two times the leading-edge radius of curvature.
Frössling [20] developed the following series expansion for h_c(s) (compressible flow, isothermal wall)

$$h_{c,FR}(s) = h_c^{stag}\Big(1 + 4\frac{u_3}{u_1}\frac{F_2'}{F_0'}\left(\frac{s}{D}\right)^2 + \\ + 6\frac{u_5}{u_1}\left(\frac{G_4'}{F_0'} + \frac{u_3^2}{u_1 u_5}\frac{H_4'}{F_0'}\right)\left(\frac{s}{D}\right)^4 + \ldots\Big) \tag{32}$$

With s/D=$\phi/2$, with ϕ the azimuthal angle measured from the stagnation point. Furthermore:

$F_0' = -0.4959 \qquad u_1 = 2(2 - \tfrac{5}{6}M_\infty^2)$

$F_2' = -0.1119 \qquad u_2 = 8(-\tfrac{1}{3} + \tfrac{77}{36}M_\infty^2)$

$G_4' = -0.0977 \qquad u_3 = 32(\tfrac{1}{60} + \tfrac{145}{144}M_\infty^2)$

$H_4' = 0.0318$

with M_∞ the free-stream Mach number.

Finally, in the stagnation point the heat convection coefficient is taken to be

$$h_c^{stag} = \frac{\kappa}{2}\left(\frac{\rho_a}{\mu_a}\frac{dU_e}{ds}\right)^{1/2} \tag{33}$$

While the Blasius expression, Eq. (31), only applies to the aft region of the airfoil, the validity of Eq. (32) is confined to a region near the stagnation point. A blending between Eq. (31) and Eq. (32) is introduced for the region in between, i.e.

$$h_c(s) = \begin{cases} h_{c,FR}(s) \\ (1-\alpha(s))h_{c,FR}(s_C) + \alpha(s)h_{c,BL}(s_{FP}) \\ h_{c,BL}(s) \end{cases} \tag{34}$$

for $s \in [0, s_C]$, $s \in [s_C, s_{FP}]$ and $s \in [s_{FP}, 1]$, respectively. In Eq. (34) $\alpha(s) = (s - s_C)/(s_{FP} - s_C)$. The coordinate s is the normalized curvilinear distance along the airfoil surface from the stag

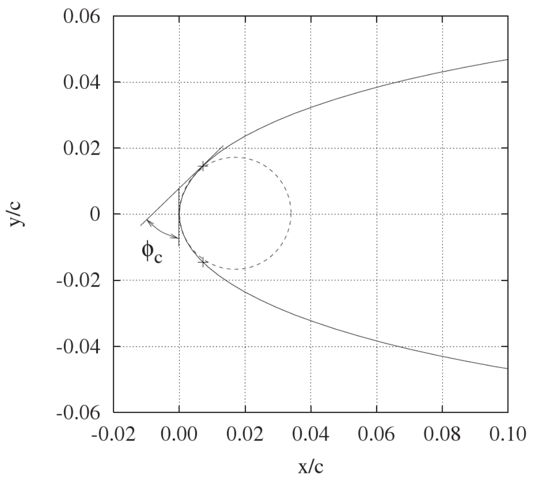

Fig. 8 Nose of NACA 0012 airfoil approximated by cylinder

nation point. s_C is defined by ϕ_C, which is set to π/4 for a NACA 0012 airfoil, see Fig.8.

Between $s = 0$ and $s = s_C$, the nose of the airfoil is approximated by a cylinder. The distance between $s = s_{FP}$ and $s = s_C$ can be modified by the user of 2DFOIL-ICE. It represents a transition region with a defined length in which the flow turns from the laminar into the fully turbulent regime.

5.5 Heat and Mass Balance

The local catching efficiency β(s) is necessary input for the ice growth model. Along with the free stream velocity $\vec{U}_\infty$ and the cloud liquid water content LWC, the catching efficiency determines how much water impinges locally on of the surface. Variations in the local catching efficiency can significantly alter the ice growth for that surface region. Using local catching efficiencies and the environmental conditions of free stream temperature, cloud liquid water content, and relative humidity, thermodynamic calculations are made which determine the rate of ice growth in each control volume along the airfoil surface. It is noted that the (shallow) control volumes of the mass and heat balances are lined up with the panels used in the panel method, except for the panel on which the stagnation point is located. The latter panel has two control volumes, one at either side of the stagnation point.

The mass balance, see Eq. (11), is

$$-\dot{m}_{in} + \dot{m}_{out} - \dot{m}_c + \dot{m}_{ev}(T) + \dot{m}_{ice} = 0 \tag{35a}$$

The heat balance, governing all three phase-regimes (Fig.2), is given in Eq. (20), as

$$\begin{aligned} \dot{m}_{ev}(T)h_{WV/IV}^{T_{ref}=T} + q_{conv}(T)\Delta s = \\ \dot{m}_c\left[c_{p,w}(T_\infty - T) + \tfrac{1}{2}U_\infty^2\right] \\ + \dot{m}_{in}\left[c_{p,w}(T_{in} - T)\right] \\ + \dot{m}_{ice}h_{IW}^{T_{ref}=T_f} - \dot{m}_{ice}c_{p,w}(T_f - T) \\ + \dot{m}_{ice}c_{p,i}(T_f - T) \end{aligned} \tag{35b}$$

For known $\dot{m}_{in}$, there are three unknowns: $\dot{m}_{out}$, $\dot{m}_{ice}$, $\dot{m}_{in}$ and $T = T_{sur}$, but only two equations. All terms in the energy balance are a function of the surface temperature. Solving Eqs. (35a) and (35b) starts at the control volume next to the stagnation point, for which $\dot{m}_{in}$ equals zero. All terms in Eq. (35b) are then evaluated for $T = T_f$ and the equation is solved for $\dot{m}_{ice}$, the rate at which ice accretes. The freezing fraction f then follows from its definition, Eq. (13).

If $0 \le f \le 1$ (phase-regime III in Fig.2), the initial guess of $T = T_f$ was correct and $\dot{m}_{out}$, the mass flow rate leaving the control volume follows from Eq. (35a).

If $f > 1$ (phase-regime II), i.e. all incoming water freezes and $\dot{m}_{ice} = \dot{m}_{in} + \dot{m}_c$. In this case, T follows from Eq. (35b).

If $f < 0$ (phase-regime I), no water freezes, i.e. $\dot{m}_{ice} = 0$ and the temperature T follows from Eq. (35b).
When the thermodynamic characteristics of the control volume are known and $\dot{m}_{ice}$ is determined, the mass balance is used to determine the mass flow rate of runback water $\dot{m}_{out}$, out of the control volume. Any water flow out of the control volume will be away from the stagnation point and into the next control volume.

The above procedure is then repeated for the adjacent downstream control volume, for which we now know $\dot{m}_{in}$, and continued along the upper surface of the airfoil. The entire procedure is then repeated again, starting at the stagnation point and proceeding along the lower surface of the airfoil.

5.6 Definition of New Ice Shape

The ice growth rate $\dot{m}_{ice}$ is assumed to apply to a certain time interval Δt. The local ice thickness follows from

$$\Delta h_{ice} = \frac{\dot{m}_{ice}\Delta t}{\rho_{ice}\Delta s} \tag{36}$$

The density rice of ice follows from an empirical relation involving the MVD, the droplet velocity at impact, the surface temperature T and the freezing temperature T_f, see [2]. The magnitude of Δt depends amongst others on the cloud liquid water content and air velocity. The time scale of the ice accretion process is much larger than the time scale of the airflow. This allows the flow conditions to be considered steady and the flow rate of the ice growth to be considered constant during an icing step.

The calculated ice thickness is added to the body in the direction normal to the surface. When the added layer thicknesses are found for all segments, the airfoil shape is updated. Subsequently, these discrete points are used in a curvature-dependent adaptive paneling scheme to accurately re-discretise the iced airfoil contour for the computation of the new velocity field. Then the calculations for a new time step are started. The flow field and the catching efficiency are re-done after each update of the iced airfoil shape, until the desired icing time has been reached.

6 Results

6.1 Single-element airfoils

To validate the ice accretion prediction capability of the 2DFOIL-ICE computational method, two single-element airfoil test cases are considered for which experimental data are available. The test case parameters are presented in Table 1, test case C-7 for a GLC305 airfoil and test case C-9 for a NLF0414 airfoil, both with a chord of 0.9144 m and the angle of attack is zero. The ambient pressure is p_∞ = 101,325 Pa. The experimental results were obtained in the NASA Glenn Icing Tunnel. Both cases are taken from the NATO/RTO TR-038 Workshop (AVT Task Group 2001), see [21]. Fig.9 shows the calculated ice shape for case C-7 and Fig.10 for case C-9. For both results one ice-step has been used. Solutions from some of the workshop participants are also included for comparison. It is noted that in our computation of the ice shape no tuning has been applied to get a closer match with the experimental ice shape, i.e. the comparison is 'blind'.

Case	U_∞ [m/s]	T_∞ [K]	*LWC* [g/m^3]	*MVD* [μm]	*Time* [s]
C-7	69.87	257.43	1.16	20	517.1
C-9	92.54	257.60	0.33	20	1224.0

Table 1 Parameters for two single-element airfoils

These results demonstrate that for these cases 2DFOIL-ICE gives results comparable to the results of other prediction methods, but agreement with the experimental results is only fair.

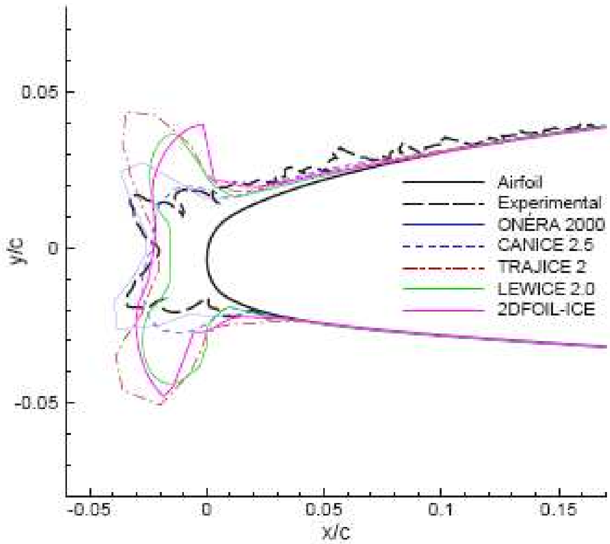

Fig. 9 Ice shapes calculated for case C-7

To validate the Eulerian method to compute the droplet collection efficiency the case is considered of the NACA0012 section at α = 0. Table 2 lists the relevant atmospheric conditions.

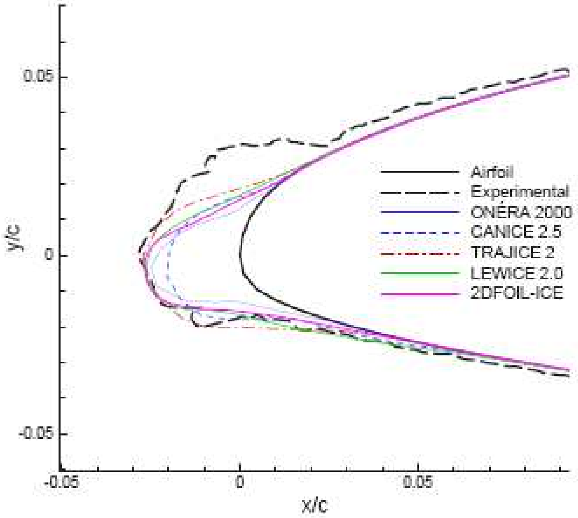

Fig. 10 Ice shapes calculated for case C-9

Case	U_∞ [m/s]	T_∞ [K]	*MVD* [μm]
NACA0012	77.0	262.74	20

Table 2 Parameters for NACA0012 validation case

The chord length is 1.0 and the ambient pressure is 101,325 Pa. First the potential-flow solution is computed using 2DFOIl-ICE with the airfoil contour discretised in 470 panels. Subsequently the collection efficiency *β(s)* is computed, via the procedure of determining the limiting droplet trajectories, etc.

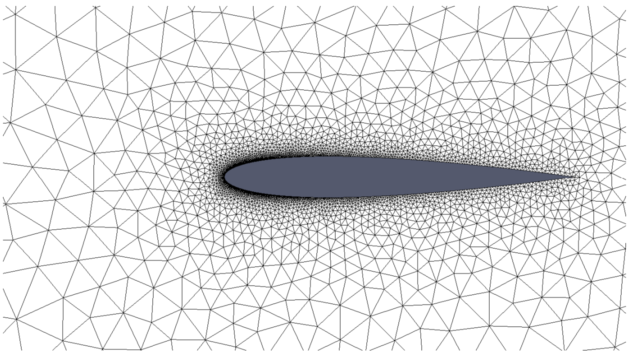

Fig. 11 Close-up of grid about NACA0012 used for computation Eulerian *β(s)*

The potential-flow solution is injected into an unstructured grid in a computational domain extending two chords upstream and two chords downstream of the airfoil. In vertical direction the domain extends one chord in either direction. The grid has around 4000 vertices and

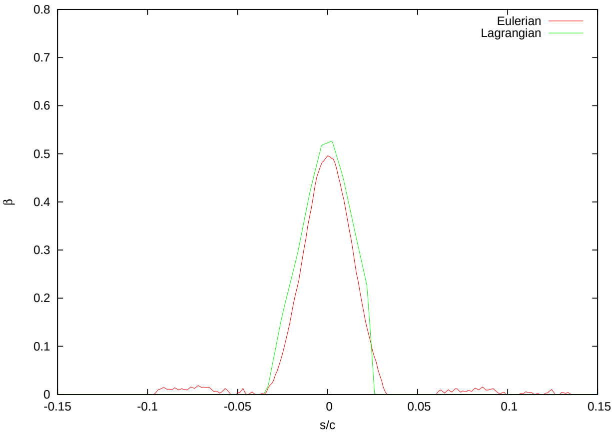

Fig. 12 NACA0012, α = 0: Distribution *β(s)* via Lagrangian and Eulerian method

7146 triangular elements. Fig. 11 shows part of the grid around the airfoil, illustrating that it is fairly easy to obtain a grid that is fine near the airfoil, but much coarser in regions where the flow velocity is more uniform. This grid is employed to compute the droplet loading Φ and droplet velocity $\vec{u}_d$, resulting in the collection efficiency *β(s)*. The results are compared in Fig. 12. It shows that the result of the Eulerian method agrees quite well with that of the Lagrangian method. However, the grid for the Eulerian method requires more surface elements than the number of panels of the Lagrangian method. Note that in the result of the Eulerian method some small spurious values of *β(s)* appear outside the wetted region. In the ice-accretion computation these values are set to zero.

6.2 Multi-element airfoil

The geometry of the airfoil is the MDA three-element airfoil used in the NATO/RTO TR-038 Workshop [21], case C-12. The chord of the airfoil is 1.0 m, with the slat and flap retracted. The ambient pressure is the atmospheric pressure at sea-level: p_∞ = 101,325 Pa

The icing conditions are given in table 3. This is a case of glaze-ice accretion, i.e. a case in which there is relatively much runback water.

Case	U_∞ [m/s]	T_∞ [K]	*LWC* [g/m^3]	*MVD* [μm]	*Time* [s]
C-12	88.4	268.2	0.6	20	360.0

Table 3 Parameters for multiple-element airfoil

The location and shape of cove bounding streamlines has been optimized for an angle of attack of 4°, it is shown in Fig. 6.

The results obtained using the potential flow method and employing the Lagrangian method to compute the droplet catching efficiency use an equidistant panel distribution on all three elements: 104 panels are used to discretise the slat, 512 panels to model the main airfoil and 207 panels to discretize the flap. Further increasing the number of panels did not lead to significantly different results.
The computed streamline pattern is shown in Fig. 13.

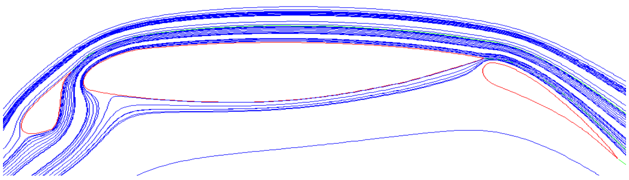

Fig. 13 2DFOIL-ICE streamline pattern around configuration shown in Fig. 6.

The streamline pattern shows the highly curved flow around the forward part of the airfoil as well as above the flap. The stagnation point on the lower surface of the main foil is also clearly shown, as well as the streamlines passing through the gap between the slat and the main airfoil element. The computed droplet trajectories are presented in Fig. 14. It shows that most of the droplets of the size considered hit the slat slightly above the stagnation point. The lower surface of the main element is wetted by the droplets in a relatively large region, as is the flap. Note that besides the droplet trajectories that impinge on the contour, some other trajectories are included to illustrate for example that the upper part of the main element, the back-end of the slat and the upper surface of the flap are not wetted by the droplets.

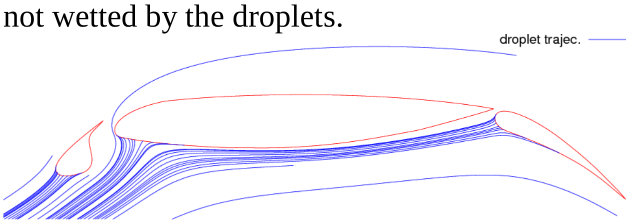

Fig. 14 2DFOIL-ICE droplet trajectories about configuration shown in Fig. 6

In Fig. 15 details of the ice accreted in 360 s as computed are compared with measured ice shapes. The predicted glaze ice shapes agree reasonably with the measured ice shapes. Both prediction and measurement indicate large regions with ice on the lower surface of the flap. The horn-like shape on the main element as computed is not seen as pronounced in the experiment, possibly caused by differences in the flow field caused by the modeling of the flow in the slat cove. Also, presumably because of a similar reason, the ice shape predicted in the gap between the main element and the flap is less extreme than in the experiment. Further note that also the free-stream line in the slat cove picks up some ice, which is of course an artifact of the present approach.

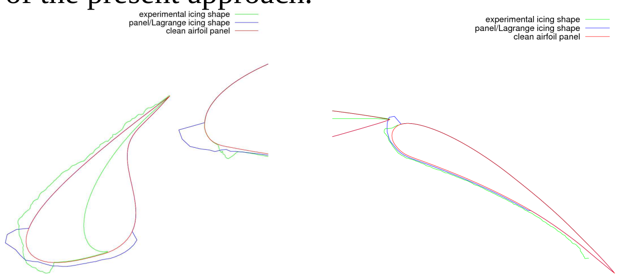

Fig. 15 2DFOIL-ICE ice shapes on configuration shown in Fig. 6. Blue line: prediction. Green line: experimental result.

The discrepancies are partly due to the cove free streamline being computed for the dry airfoil only, and to the ice-accretion prediction being based one time step only.

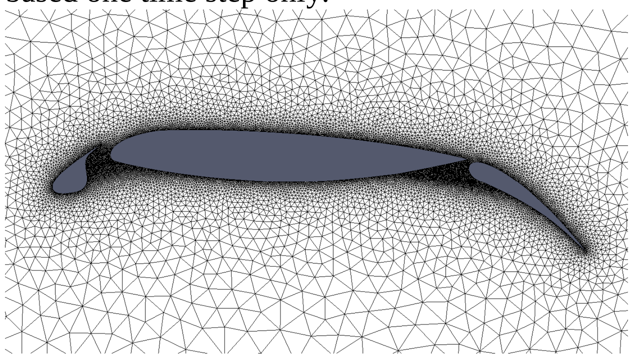

Fig. 16 Close-up of grid about C-12 configuration used for Euler flow solution and for the Eulerian computation of $\beta(s)$

Fig. 16 presents the unstructured grid used to obtain the solution of the Euler flow equations.

Note that the geometry with the faired-over coves of Fig. 6 is used. The computational domain extends one chord in upstream, one chord in downstream and one chord both below and above the airfoil. The upper and lower boundaries of the domain are free-slip walls. The grid contains about 12,500 nodes and 23,500 triangles. The grid is refined near the surface of the configuration and specifically in the region between the slat and the main element and the region between the main element and the flap. The streamline pattern obtained from the Euler solution is shown in Fig. 17.

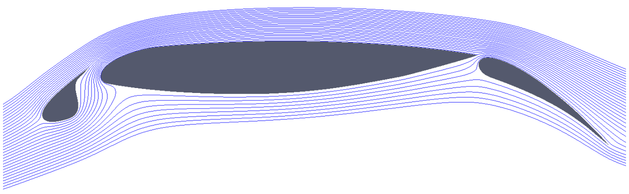

Fig. 17 EFD-FLOW streamline pattern around configuration shown in Fig. 6.

This picture is quite similar to the streamline pattern shown in Fig. 13 that was obtained from the potential-flow solution. There is some difference in the location of the stagnation points, but the general agreement is good, considering the presence of walls for the Euler solution.

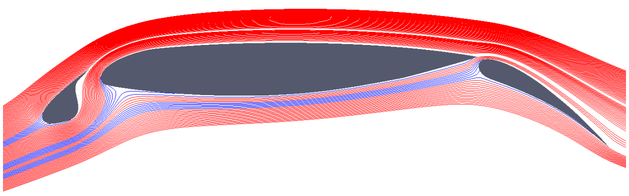

Fig. 18 Droplet trajectories around configuration shown in Fig. 6. Flow computed with EFD-FLOW, droplet velocity field from Lagrangian method. Red: non-impinging; blue: impinging trajectories.

Fig. 18 shows the droplet trajectories computed from the droplet velocity field employing the Lagrangian method. Comparison of Fig. 14 with Fig 18 (blue curves) shows a very similar pattern. More pronounced in Fig. 18 is that the whole lower side of the flap (and to a lesser extent the lower side of the main element) appears to be wetted by the droplets. Furthermore, note that the near the leading edge the flap is also wetted on its upper side.

Fig. 19 shows the droplet catching efficiency β, as function of x/c, on the slat, the main element and the flap. The (red) result of the potential-flow method coupled with the Lagrangian method for the droplet trajectories is compared with the (blue) result of the Euler method coupled with the Eulerian method for the droplet trajectories. On the slat about the same region is wetted, but the result of the potential-flow method coupled with Lagrangian indicates that more wetting takes place than obtained with the Euler/Eulerian method. Fig. 19 shows a similar result, with the main element collecting about the same amount of water as the slat and the flap. On the main element Euler/Eulerian yields a larger wetted area. For the flap the two results differ in a similar way, with the Euler/Eulerian method giving wetting over a larger region.

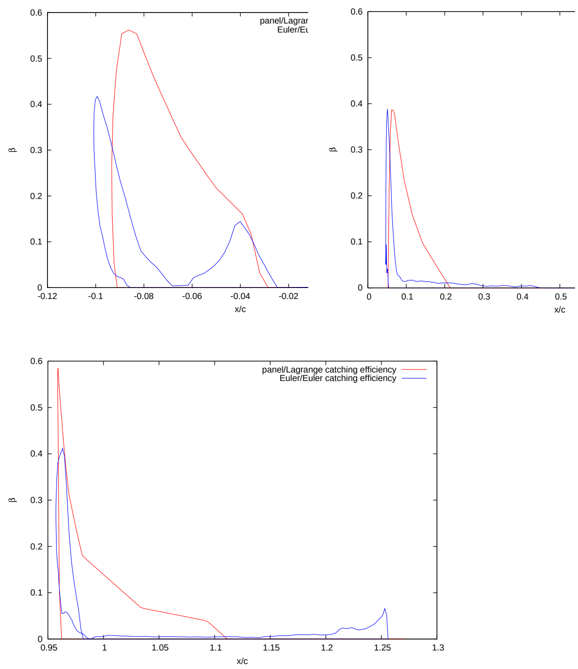

Fig. 19 Droplet catching efficiency on configuration shown in Fig. 6. Upper left: slat; upper right: main element; lower: flap. Red: potential flow + Lagrangian. Blue: Euler solution + Eulerian.

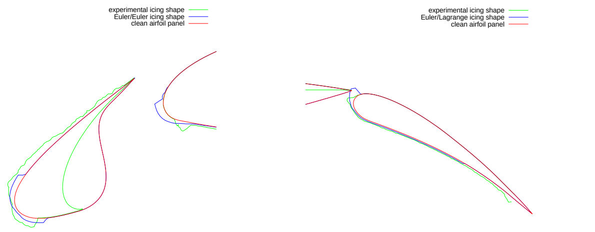

Fig. 20 Ice shapes predicted with EFD-FLOW+-Eulerian droplet catching efficiency method for configuration shown in Fig. 6. Blue: prediction, green: experiment.

Fig. 20 shows the ice accretion shapes predicted employing the method in which the flow field is computed by solving the Euler equations on an unstructured grid and the droplet catching efficiency is derived from the solution of the droplet loading and droplet velocity computed on the same unstructured grid. The prediction is compared with experimental results from [21], showing a fair agreement. Also the comparison of the ice accretions in Fig. 15, obtained with the potential flow method coupled with Lagrangian droplet catching reveals a fair comparison, in spite of the considerable differences in the droplet catching efficiency.

7 Concluding Remarks

In this study, computational methods have been presented that compute ice accretion on (multiple-element) airfoils in specified icing conditions. For single-element airfoils calculated ice shapes have been compared with experimental results that were obtained in the NASA Glenn Icing Tunnel and with numerical results from other ice accretion prediction methods. A good agreement is found with the rime and glaze-ice shapes predicted by other computational methods. Agreement with the experimental ice shapes is fair.
The ice accretion process occurring on a three-element airfoil is much more complex than that on a single-element airfoil. Both methods used to compute the flow field, i.e. the potential-flow method and the Euler method necessitate the modeling of the separated flow in the cove regions. This introduces an uncertainty in the prediction.

It is shown that, given the same flow field, the Lagrangian method to compute the droplet catching efficiency from droplet tracking gives results comparable to those of the Eulerian method that determines the droplet catching efficiency from the field of the droplet loading and that of the droplet velocity, obtained on an unstructured grid. Comparison with experimental data indicates a fair agreement.

The method can be improved by implementing a better model of the external boundary layer. Solving the boundary layer equations with an integral method might give a better prediction of the friction coefficient and the heat transfer coefficient than using the local value of the velocity in the flat-plate boundary-layer relations. Extension of the unstructured Euler method to a method solving the Navier-Stokes equations would be a next step.

References

[1] Petty K.R. and Floyd C.D.J. *A statistical review of aviation airframe icing accidents in the US.* National Transportation Safety Board, Washington, D.C., 2004.

[2] Snellen M., Boelens O.J. and Hoeijmakers H.W.M. A computational method for numerically simulating ice accretion. AIAA Paper 97-2206, Jan. 1997.

[3] Dillingh J.E., Hoeijmakers H.W.M. Simulation of ice accretion on airfoils during flight., *FAA In-Flight Icing/Ground De-Icing International Conference & Exhibition, SAE*, SAE Paper 2003-01-2137, Chicago, Illinois, USA, June 2003, 12 pages.

[4] Dillingh J.E. and Hoeijmakers H.W.M. Numerical simulation of airfoil ice accretion and thermal anti-icing systems. *24th International Congress of Aeronautical Sciences*, Yokohama, Japan, CD-Rom, ISBN 0-953391-6-8, 12 pages, 2004

[5] Jacobs S.J. *Icing Simulation, Prediction of Ice Accretion on Multi-element Airfoils using a Panel Method.* MSc thesis, University of Twente, Enschede, the Netherlands, 2005.

[6] Messinger B. Equilibrium temperature of an unheated icing surface as a function of air speed. *J. of Aeron. Sciences*, Vol. 20, No. 1, Jan. 1953.

[7] Vukits T. Overview and risk assessment of icing for transport category aircraft and components. AIAA Paper 2002-0811, Jan. 2002.

[8] Kelleners P.H. *An edge-based finite volume method for inviscid compressible flow with condensation.*

PhD thesis, University of Twente, Enschede, the Netherlands, 2007.

[9] Koop A.H. *Numerical simulation of unsteady three-dimensional sheet cavitation.* PhD thesis, University of Twente, Enschede, the Netherlands, 2008.

[10] Harten A, Lax P.D. and van Leer B. On upstream differencing and Godunov-type schemes for hyperbolic conservation laws. *Siam Reviews*, Vol.. 25, pp. 35-61 (1983).

[11] Toro E.F., Spruce M. and Speares W. Restoration of the contact surface in the HLL-Riemann solver. *Shock Waves,* Vol. 4, pp. 25-34 (1994)

[12] Batten P., Clarke N., Lambert C. and Causon D.M. On the choice of wave speeds for the HLLC Riemann solver. *Siam J. Sci. Comput.,* Vol. 18, pp. 1553-1570 (1997).

[13] Liou M.S. and Steffen J. A new flux-splitting scheme. *J. Comput Physic.,* Vol. 107, pp. 23-39 (1993).

[14] Liou M.S. A sequel to AUSM: AUSM+. *J. Comput Physic.,* Vol. 129, pp. 364-382 (1996).

[15] Liou M.S. A sequel to AUSM, Part II: AUSM+-up for all speeds. *J. Comput Physic.*, Vol. 214, pp. 137-170 (2006).

[16] Leer B. van. Towards the ultimate conservative difference scheme V. A second-order sequel to Godunov’s method. *J. Comput Phys.*, Vol. 32, pp. 101-136 (1979).

[17] Barth T.J. and Jespersen D.C. The design and application of upwind schemes on unstructured meshes. AIAA Paper 89-0366, Jan. 1989.

[18] Venkatakrishnan V. Convergence to steady-state solutions of the Euler equations on unstructured grids with limiters. *J. Comput Phys.*, Vol. 118, pp. 120-130 (1995).

[19] Bourgault Y., Habashi W.G., Dompierre J. and Baruzzi A finite element method study of Eulerian droplets impingement models. *Int. J. Numer. Meth. Fluids* Vol. 29, pp. 429-449 (1999).

[20] Frössling N. *Evaporation, heat transfer and velocity distribution in two-dimensional and rotationally symmetrical laminar boundary-layer flow*. Technical Memorandum 1432, NACA, 1958.

[21] Kind R.J. *Ice accretion simulation evaluation test.* NATO/RTO TR 038, AVT Task Group 006, November 2001.

Copyright Statement